


 Cite this: *RSC Adv.*, 2018, **8**, 33035

Synthesis, structure, and luminescence characteristics of far-red emitting Mn^{4+} -activated $LaScO_3$ perovskite phosphors for plant growth

Liangling Sun, Balaji Devakumar, Heng Guo, Jia Liang, Bin Li, Shaoying Wang, Qi Sun and Xiaoyong Huang *

Far-red emitting phosphors $LaScO_3:Mn^{4+}$ were successfully synthesized via a high-temperature solid-state reaction method. The X-ray powder diffraction confirmed that the pure-phase $LaScO_3:Mn^{4+}$ phosphors had formed. Under 398 nm excitation, the $LaScO_3:Mn^{4+}$ phosphors emitted far red light within the range of 650–800 nm peaking at 703 nm ($14\,225\,cm^{-1}$) due to the $^2E_g \rightarrow ^4A_{2g}$ transition, which was close to the spectral absorption center of phytochrome P_{FR} located at around 730 nm. The optimal doping concentration and luminescence concentration quenching mechanism of $LaScO_3:Mn^{4+}$ phosphors was found to be 0.001 and electric dipole–dipole interaction, respectively. And the CIE chromaticity coordinates of the $LaScO_3:0.001Mn^{4+}$ phosphor were (0.7324, 0.2676). The decay lifetimes of the $LaScO_3:Mn^{4+}$ phosphors gradually decreased from 0.149 to 0.126 ms when the Mn^{4+} doping concentration increased from 0.05 to 0.9 mol%. Crystal field analysis showed that the Mn^{4+} ions experienced a strong crystal field in the $LaScO_3$ host. The research conducted on the $LaScO_3:Mn^{4+}$ phosphors illustrated their potential application in plant lighting to control or regulate plant growth.

 Received 7th August 2018
 Accepted 19th September 2018

 DOI: 10.1039/c8ra06629a
rsc.li/rsc-advances

Introduction

Nowadays, to meet the continuous increasing needs of people, the greenhouse industry has been developed. In the agriculture field, when it comes to conditions for plant growth, moderate sunlight, air, and moderate moisture are usually mentioned as the basic conditions.^{1–4} The blue (≈ 400 –500 nm), red (≈ 600 –690 nm) and far red (≈ 700 –740 nm) light in sunlight can affect the growth process of natural plants, such as phototropic processes and photomorphogenesis.^{5–7} There exist two kinds of phytochrome, P_R and P_{FR} , and P_R is the biologically inactive state, whereas P_{FR} is the biologically active state.^{4,8} These two phytochromes can be converted into each other by absorbing different wavelengths of light, in which the P_R was sensitive to red light and can turn into P_{FR} by absorbing light with wavelength peaking at around 660 nm, whereas P_{FR} should absorb far red light peaking at around 730 nm to switch to P_R .^{9,10} It is known that in order to blossom, short-day plants need to stay in the dark for a longer time than long-day plants.^{11–13} So plant growth progress can be controlled by changing the spectral composition in artificial light.

The proportion of red light in the natural sunlight is higher than far red light.⁹ Meanwhile, with the development of science and technology in the world, the far red light become even less due to the night lighting, which means the far-red light is

insufficient for plant cultivation and even influence the entire life style of the plant.⁴ Thus, finding artificial light to meet the requirement of plant growth is urgent, especially in the greenhouse industry. In the past, the light emitted by traditional gas-discharge lamps cannot match well with the absorption spectrum of phytochrome, especially the P_{FR} . But the solid state light-emitting diodes (LEDs) device with long lifetime and low power consumption,^{14–21} which can exhibit various colors by coating different phosphors onto the blue/near-ultraviolet LED chip,^{22–30} can make up for this drawback. That means the light from the specific LEDs can match well with the absorption spectrum of phytochrome. Many research efforts have already been conducted to develop the red phosphors, such as $K_2NaAlF_6:Mn^{4+}$ (630 nm),³¹ $Na_3MgZr(PO_4)_3:Eu^{3+}$ (611 nm),³² and $Sr_2MgAl_2O_6:Mn^{4+}$ (658 nm),³³ which emit red light in the range of 610–660 nm. In contrast, relatively less attention has been paid to the far-red phosphors with emission wavelength within 660–730 nm, which can be used for the plant growth. So it is important to find novel phosphors that can emit far-red light to meet the requirement of far-red light.

Mn^{4+} ions in particular host materials with octahedral structures can emit red light and even deep red light due to the $^2E_g \rightarrow ^4A_{2g}$ transition,^{34–37} such as $Sr_4Al_{14}O_{25}:Mn^{4+}$ (652 nm),³⁸ $NaMgGdTeO_6:Mn^{4+}$ (697 nm),³⁹ $Ca_3La_2W_2O_{12}:Mn^{4+}$ (711 nm),⁴⁰ $La_2MTiO_6:Mn^{4+}$ ($M = Mg$ and Zn ; 710 nm),⁴¹ and $Ba_2GeO_4:Mn^{4+}$ (667 nm).⁴² Considering that the structure of the $LaScO_3$ compound with $[ScO_6]$ octahedral structure is similar to $LaAlO_3$ and Mn^{4+} -doped $LaAlO_3$ phosphors can emit far-red emission,

College of Physics and Optoelectronics, Taiyuan University of Technology, Taiyuan 030024, PR China. E-mail: huangxy04@126.com



so the LaScO_3 compound has been chosen as the host for Mn^{4+} doping.^{43,44} Thus, in this work, LaScO_3 and Mn^{4+} ions had been chosen for the host material and activator, respectively, and a series of $\text{LaScO}_3:\text{xMn}^{4+}$ ($x = 0.0005\text{--}0.009$) phosphors with different Mn^{4+} doping concentration had been synthesized. These prepared phosphors can be well excited by 398 nm and emit far-red light peaking at 703 nm with CIE chromaticity coordinates of (0.7324, 0.2676). The crystal structure of the LaScO_3 , decay lifetimes and luminescence properties had also been investigated in detail, and the results indicated the $\text{LaScO}_3:\text{Mn}^{4+}$ phosphors could be serve as the far-red emitting phosphor in plant growth LEDs.

Experimental section

$\text{LaScO}_3:\text{xMn}^{4+}$ ($x = 0.0005\text{--}0.009$) phosphors were prepared by a facile solid-state reaction method using Sc_2O_3 (analytical reagent, AR), MnCO_3 (AR), and La_2O_3 (99.99%) as the starting materials. The raw materials were weighed according to the stoichiometric ratio. The mixed starting materials was ground in an agate mortar and transferred to Al_2O_3 crucible to sinter at 1500 °C for 10 h in air. And then, the products were cooled down to room temperature and reground into powders to get the target phosphors $\text{LaScO}_3:\text{xMn}^{4+}$.

The X-ray powder diffraction (XRD) results of $\text{LaScO}_3:\text{xMn}^{4+}$ phosphors were measured on an X-ray diffractometer (Bruker D8 Advance) with $\text{Cu-K}\alpha$ radiation. The room-temperature photoluminescence (PL)/PL excitation (PLE) spectra and luminescence decay lifetimes of $\text{LaScO}_3:\text{xMn}^{4+}$ phosphors were recorded by using the same Edinburgh FS5 spectrofluorometer, equipping with a 150 W continued-wavelength Xenon lamp and a pulsed Xenon lamp, respectively. The internal quantum efficiency (IQE) of the $\text{LaScO}_3:0.001\text{Mn}^{4+}$ phosphors were measured by the Edinburgh FS5 spectrofluorometer with a integrating sphere.

Results and discussion

Fig. 1 showed the XRD patterns of the $\text{LaScO}_3:\text{xMn}^{4+}$ ($x = 0, 0.0005, 0.001$, and 0.005) phosphors and the standard data of LaScO_3 (JCPDS: 26–1148). It could be seen that all the diffraction peaks of the samples matched well with the standard data of LaScO_3 . There was no excess crystal phase formation, which illustrated the Mn^{4+} ions could be successfully doped into the LaScO_3 host. Mn^{4+} ions can replace specific cationic sites of the specific host, where cationic sites have a coordination number (CN) of six, such as Nb^{5+} , Zr^{4+} , Ti^{4+} , Te^{6+} , and W^{6+} ions.^{39,40,45–48} Considering the cationic radius and the coordination environment of Mn^{4+} ($r = 0.535 \text{ \AA}$, CN = 6) and Sc^{3+} ($r = 0.745 \text{ \AA}$, CN = 6),^{43,49,50} the Mn^{4+} ions could replace the Sc^{3+} sites in the LaScO_3 host.

In order to identify the structure of the as-prepared sample, the Rietveld refinement for the LaScO_3 host and $\text{LaScO}_3:0.001\text{Mn}^{4+}$ phosphors were conducted. Fig. 2(a) and (b) depict the Rietveld refinement results of LaScO_3 host and $\text{LaScO}_3:0.001\text{Mn}^{4+}$, respectively. From the values of R_p and R_{wp} ($R_p = 8.13\%$ and $R_{wp} = 7.55\%$ for LaScO_3 host; $R_p = 4.86\%$ and $R_{wp} = 3.50\%$

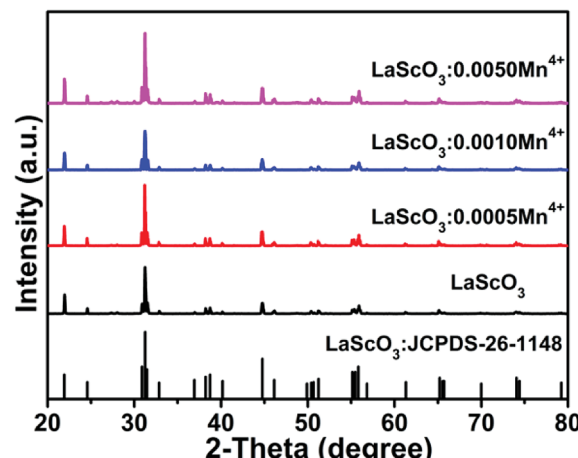


Fig. 1 XRD patterns of $\text{LaScO}_3:\text{xMn}^{4+}$ ($x = 0, 0.0005, 0.001$, and 0.005) phosphors and the stand pattern of LaScO_3 (JCPDS: 26–1148).

for $\text{LaScO}_3:0.001\text{Mn}^{4+}$ phosphors), we could know that the obtained results were reliable. The refined crystallographic parameters of the LaScO_3 host and $\text{LaScO}_3:0.001\text{Mn}^{4+}$ phosphors were listed in Table 1 and Table 2, respectively. It could be seen that the parameters of LaScO_3 host and $\text{LaScO}_3:0.001\text{Mn}^{4+}$ phosphors changed slightly due to the difference in ions radii between Sc^{3+} and Mn^{4+} ions. The crystal systems of the LaScO_3 host and $\text{LaScO}_3:0.001\text{Mn}^{4+}$ phosphors were orthorhombic with a space group of $Pbnm$. Fig. 2(c) and (d) show the crystal structure of the LaScO_3 host and the $[\text{ScO}_6]$ octahedron, respectively. In the unit cell, one Sc^{3+} ion was surrounded by six O^{2-} ions to form $[\text{ScO}_6]$ octahedral units and the Mn^{4+} ions could substitute for Sc^{3+} ions to form the $\text{LaScO}_3:\text{Mn}^{4+}$ compound. All the results illustrated the formation of $\text{LaScO}_3:\text{Mn}^{4+}$ phosphors.

The PLE and PL spectra of the $\text{LaScO}_3:0.001\text{Mn}^{4+}$ phosphors were shown in Fig. 3(a). When monitored at 703 nm, the obtained excitation spectrum of the Mn^{4+} ions in LaScO_3 was an asymmetric absorption band, which could be fitted to four peaks though Gaussian fitting, namely, peaks at 346 nm ($28\ 902 \text{ cm}^{-1}$; $\text{Mn}^{4+}\text{--O}^{2-}$ transition), 392 nm ($25\ 510 \text{ cm}^{-1}$; ${}^4\text{A}_{2g} \rightarrow {}^4\text{T}_{1g}$ dominant transition), 462 nm ($21\ 645 \text{ cm}^{-1}$; ${}^4\text{A}_{2g} \rightarrow {}^2\text{T}_{2g}$ transition), and 543 nm ($18\ 416 \text{ cm}^{-1}$; ${}^4\text{A}_{2g} \rightarrow {}^4\text{T}_{2g}$ transition).^{48,51} Under the excitation of 398 nm or 549 nm, the $\text{LaScO}_3:0.001\text{Mn}^{4+}$ phosphors emitted deep red light peaking at 703 nm (${}^2\text{E}_g \rightarrow {}^4\text{A}_{2g}$ transition; see Fig. 3(a)) with the CIE chromaticity coordinates of (0.7324, 0.2676) (see Fig. 3(b)). Fig. 3(c) shows the absorption spectra of P_R and P_{FR} as well as the emission spectrum of the $\text{LaScO}_3:0.001\text{Mn}^{4+}$ phosphor. Obviously, the PL spectrum of the $\text{LaScO}_3:0.001\text{Mn}^{4+}$ phosphor was located within the absorption spectrum of the P_{FR} . Importantly, the dominant emission peak of $\text{LaScO}_3:0.001\text{Mn}^{4+}$ phosphor at 703 nm was close to the peak wavelength (around 730 nm) of the absorption spectrum of P_{FR} . So it was meaningful to apply $\text{LaScO}_3:\text{Mn}^{4+}$ phosphors to plant growth LEDs.

To find the optimal doping concentration of Mn^{4+} ions in $\text{LaScO}_3:\text{Mn}^{4+}$ phosphors, a series of $\text{LaScO}_3:\text{xMn}^{4+}$ ($x = 0.0005\text{--}0.009$) phosphors were synthesized and the corresponding PL



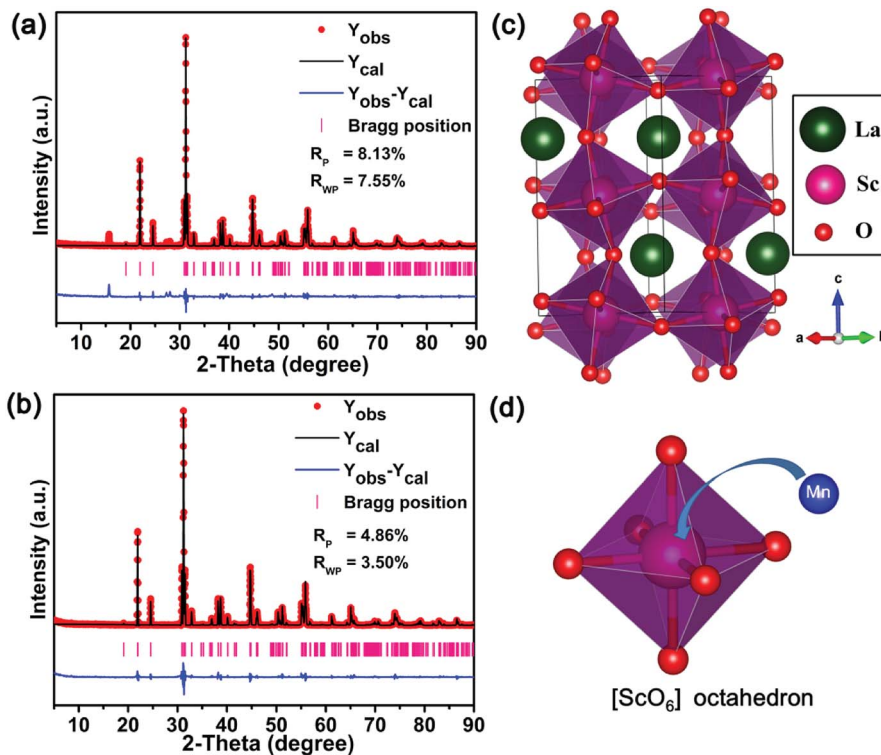


Fig. 2 Rietveld refinement of LaScO_3 host (a) and $\text{LaScO}_3:0.001\text{Mn}^{4+}$ (b) using the Fullprof suit software. The structure of (c) LaScO_3 host and (d) $[\text{ScO}_6]$ octahedron.

spectra were shown in Fig. 3(d). It could be found that the PL intensity of the $\text{LaScO}_3:x\text{Mn}^{4+}$ phosphors firstly increased as Mn^{4+} concentration increased and then decreased, and the optimal-doping concentration reached when $x = 0.001$, which was attributed to the concentration quenching in the $\text{LaScO}_3:x\text{Mn}^{4+}$ phosphors. The IQE of the $\text{LaScO}_3:0.001\text{Mn}^{4+}$ phosphor was 15%. The optical doping concentration of Mn^{4+} is much lower than rare-earth doped phosphors, because the d-electron wave functions of transition metals (e.g., Mn^{4+} ions) extend more widely than 4f electrons of rare earths (e.g., Eu^{3+} and Tb^{3+} ions).^{52,53} Due to the energy transfer between the nearest Mn^{4+} and ends with energy transfer to traps or killing sites,

concentration quenching occurs in $\text{LaScO}_3:x\text{Mn}^{4+}$ phosphors.^{47,54} Considering the concentration quenching occurred in $\text{LaScO}_3:x\text{Mn}^{4+}$ phosphors, the critical distance (R_c) of Mn^{4+} ions in the $\text{LaScO}_3:x\text{Mn}^{4+}$ phosphors was calculated using the following equation:^{55,56}

$$R_c = 2 \left(\frac{3V}{4\pi x_c N} \right)^{1/3} \quad (1)$$

where V and N represents the volume and the number of host cations of the unit cell, respectively; x_c refers to the optimal doping concentration of Mn^{4+} ions. Herewith, $V = 266.251(14)$ \AA^3 , $N = 4$, and $x_c = 0.001$. Hence, the R_c of Mn^{4+} ions in

Table 1 Refined crystallographic parameters of LaScO_3 host

Formula	LaScO_3									
Crystal system	Orthorhombic									
Space group	$pbnm$									
Lattice parameters	$a = 5.68010(17)$ \AA , $b = 5.79022(16)$ \AA , $c = 8.0952(2)$ \AA , $V = 266.244(13)$ \AA^3									
Atom	$U_{\text{aniso}} (\text{\AA}^2)$									
	x	y	z	Occ.	U_{11}	U_{22}	U_{33}	U_{12}	U_{13}	U_{23}
La1	0.01060	0.95680	0.25	1	0.01218	0.00649	-0.00259	-0.00656	0.00000	0.00000
Sc1	0.00000	0.5	0.00000	1	0.00448	-0.00362	0.00289	-0.00681	-0.00587	-0.00140
O1	0.71276	0.28618	0.01023	1	-0.05698	0.04639	-0.04425	-0.01988	0.00000	0.00000
O2	0.90808	0.52065	-0.01828	1	0.04604	-0.02305	0.00770	0.02371	0.02416	0.03004



Table 2 Refined crystallographic parameters of $\text{LaScO}_3:0.001\text{Mn}^{4+}$ phosphors

Formula	$\text{LaScO}_3:0.001\text{Mn}^{4+}$									
Crystal system	Orthorhombic									
Space group	$pbnm$									
Lattice parameters	$a = 5.67879(18) \text{ \AA}$, $b = 5.79140(16) \text{ \AA}$, $c = 8.0956(3)$, $V = 266.251(14) \text{ \AA}^3$									
	$U_{\text{aniso}} (\text{\AA}^2)$									
Atom	x	y	z	Occ.	U_{11}	U_{22}	U_{33}	U_{12}	U_{13}	U_{23}
La1	0.00909	0.95617	0.25	1	0.00781	-0.00411	0.00299	-0.00040	0.00000	0.00000
Sc1	0.00000	0.5	0.00000	0.999	0.01333	-0.00843	-0.00312	0.00057	0.00554	-0.00207
Mn1	0.00000	0.5	0.00000	0.001	0.01333	-0.00843	-0.00312	0.00057	0.00554	-0.00207
O1	0.91109	0.52509	0.25000	1	-0.00405	-0.02970	-0.00531	-0.00072	0.00000	0.00000
O2	0.70010	0.30343	0.01124	1	0.02081	0.03995	-0.02703	-0.02709	-0.00394	0.00625

$\text{LaScO}_3:x\text{Mn}^{4+}$ was calculated to be about 50.29 \AA ($>5 \text{ \AA}$), which was comparable with that in other Mn^{4+} doped phosphors, such as $\text{KMgLaTeO}_6:\text{Mn}^{4+}$ (33.83 \AA),⁵⁷ $\text{Ba}_2\text{TiGe}_2\text{O}_8:\text{Mn}^{4+}$ (40.1 \AA),⁴⁹ $\text{Li}_2\text{MgZrO}_4:\text{Mn}^{4+}$ (33.8 \AA),⁴⁸ indicating that the luminescence concentration quenching derived from the electric multipole interaction.²⁵

To determine whether the electric multipole interaction was electric dipole-dipole (d-d), or dipole-quadrupole (d-q), or quadrupole-quadrupole (q-q) interactions, the following equation could be used to get the exact form:^{58,59}

$$\frac{I}{x} = k \left[1 + \beta(x)^{\theta/3} \right]^{-1} \quad (2)$$

where I represents the PL intensity; β and k are constants for a given host lattice; $\theta = 6, 8$ and 10 stands for electric d-d, d-q, and q-q interactions, respectively; x is the dopant content of Mn^{4+} ions in LaScO_3 host. The relationship between $\log(I/x)$ and $\log(x)$ was plotted in Fig. 3(e) and the slope of the fitting result was found to be -1.71990 ($=-\theta/3$), revealing that the value of θ was about 5.16. Thus, the luminescence concentration quenching mechanism of Mn^{4+} ions in LaScO_3 host was electric d-d interaction.

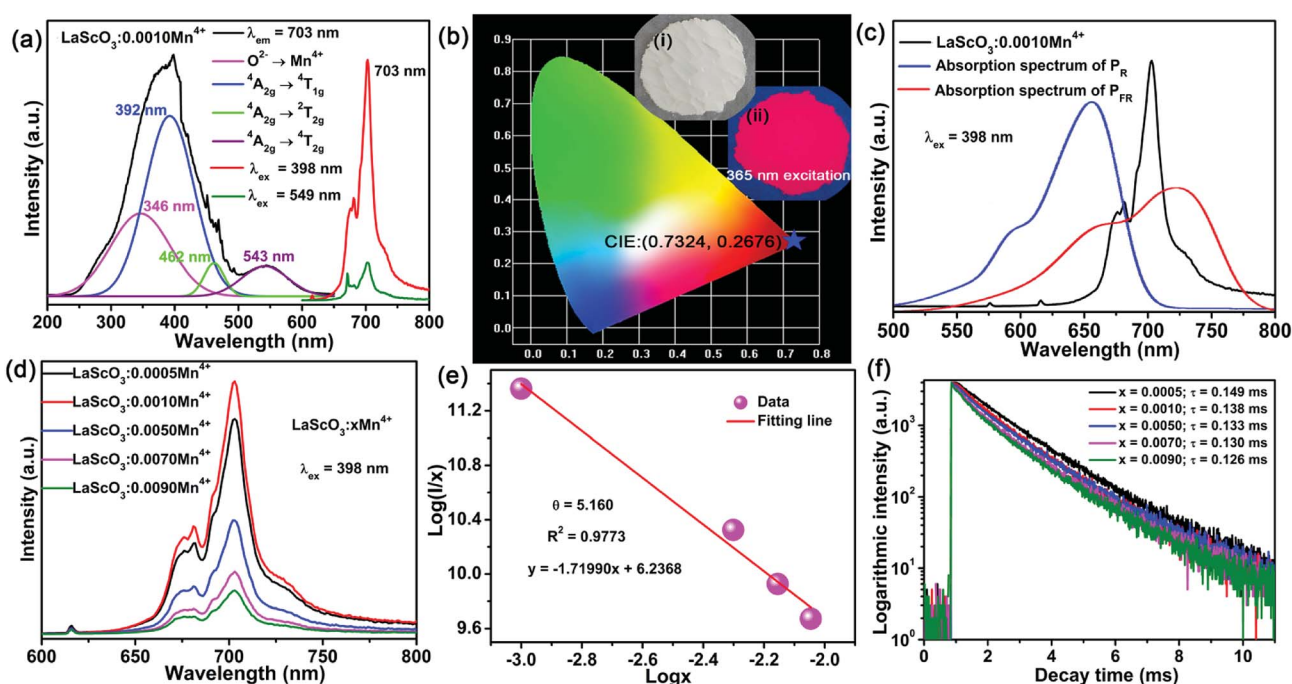


Fig. 3 (a) The PLE spectrum of $\text{LaScO}_3:0.001\text{Mn}^{4+}$ phosphors monitored at 703 nm . The four curves represent the Gaussian fitting curves. (b) The CIE chromaticity diagram of $\text{LaScO}_3:0.001\text{Mn}^{4+}$ phosphors. The insets show the phosphor digital pictures under the 365 nm excitation (ii) and daylight (i). (c) The room-temperature PL spectrum of $\text{LaScO}_3:0.001\text{Mn}^{4+}$ sample excited at 398 nm and the absorption spectra of phytochrome P_R and P_{FR} . (d) The PL spectra of $\text{LaScO}_3:x\text{Mn}^{4+}$ ($x = 0.0005\text{--}0.009$) phosphors excited at 398 nm . (e) Plot of $\log(I/x)$ vs. $\log(x)$ of Mn^{4+} ions in $\text{LaScO}_3:x\text{Mn}^{4+}$ phosphors. (f) The luminescence decay curves of $\text{LaScO}_3:x\text{Mn}^{4+}$ ($x = 0.0005\text{--}0.009$) phosphors under the test condition of $\lambda_{\text{em}} = 703 \text{ nm}$ and $\lambda_{\text{ex}} = 398 \text{ nm}$.



Fig. 3(f) exhibits the luminescence decay curves of Mn^{4+} 703 nm emissions in $\text{LaScO}_3:\text{xMn}^{4+}$ ($x = 0.0005\text{--}0.009$) phosphors. The decay lifetimes of the $\text{LaScO}_3:\text{xMn}^{4+}$ samples were obtained by the following double-exponential model:⁶⁰

$$I = A_1 \exp(-t/\tau_1) + A_2 \exp(-t/\tau_2) \quad (3)$$

where I refers to the luminescent emission intensities at time t ; A_1 and A_2 are constants; and τ_1 and τ_2 are the decay time for the exponential component, respectively. The decay lifetimes of the $\text{LaScO}_3:\text{xMn}^{4+}$ phosphors were calculated to be 0.149 ms ($x = 0.0005$), 0.138 ms ($x = 0.001$), 0.133 ms ($x = 0.005$), 0.130 ms ($x = 0.007$), and 0.126 ms ($x = 0.009$). Obviously, the decay lifetimes decreased as the concentration x increased, revealing the non-radiative energy-migration of Mn^{4+} ions in the $\text{LaScO}_3:\text{xMn}^{4+}$ phosphors.

To explore the influence of the octahedral coordination environment of $\text{LaScO}_3:\text{xMn}^{4+}$ phosphors on the $3d^3$ energy level of Mn^{4+} ions, Fig. 4(b) shows the Tanabe–Sugano energy-level diagram of Mn^{4+} ions in the octahedral site of LaScO_3 host together with the simple energy level diagram of Mn^{4+} ions. Based on the ${}^4\text{A}_{2g} \rightarrow {}^4\text{T}_{2g}$ ($18\,416\text{ cm}^{-1}$) transition energy gap, the crystal-field strength (Dq) of the $\text{LaScO}_3:\text{xMn}^{4+}$ phosphors can be roughly estimated by the following equation:⁶¹

$$Dq = E({}^4\text{A}_{2g} \rightarrow {}^4\text{T}_{2g})/10 \quad (4)$$

Based on the PLE spectrum of the $\text{LaScO}_3:0.001\text{Mn}^{4+}$ phosphors, the energy difference between the ${}^4\text{A}_{2g} \rightarrow {}^4\text{T}_{1g}$ ($25\,510\text{ cm}^{-1}$) and ${}^4\text{A}_{2g} \rightarrow {}^4\text{T}_{2g}$ ($18\,416\text{ cm}^{-1}$) was about 7094 cm^{-1} . Therefore, the Racah parameter B can be obtained by the following expression:⁶²

$$\frac{Dq}{B} = \frac{15(x-8)}{(x^2-10x)} \quad (5)$$

in which the x can be calculated by:

$$x = \frac{E({}^4\text{A}_{2g} \rightarrow {}^4\text{T}_{1g}) - E({}^4\text{A}_{2g} \rightarrow {}^4\text{T}_{2g})}{Dq} \quad (6)$$

From the PL spectrum of the $\text{LaScO}_3:0.001\text{Mn}^{4+}$ phosphors, the energy of the ${}^2\text{E}_g \rightarrow {}^4\text{A}_{2g}$ ($14\,225\text{ cm}^{-1}$) was acquired and the Racah parameter B was evaluated by the following expression:^{47,63}

$$\frac{E({}^4\text{E}_g \rightarrow {}^4\text{A}_{2g})}{B} = \frac{3.05C}{B} + 7.9 - \frac{1.8B}{Dq} \quad (7)$$

According to the eqn (4)–(7), the crystal field parameters Dq , B , and C were 1842, 701, and 3006 cm^{-1} , respectively. Thus the value of the Dq/B , which represented the intensity of the crystal field, was about 2.628 (>2.2), indicating that the Mn^{4+} ions experienced strong crystal strength in LaScO_3 host than those in $\text{Y}_3\text{Al}_5\text{O}_12$ ($Dq/B = 1.98$),⁶⁴ Ba_2YSbO_6 ($Dq/B = 1.88$),⁶⁵ and $\text{Ca}_2\text{LaNbO}_6$ ($Dq/B = 2.31$).⁶⁶

The emission energy of the ${}^2\text{E}_g \rightarrow {}^4\text{A}_{2g}$ transition of Mn^{4+} ions in specific host could be affected by the nephelauxetic effect.⁶⁷ The nephelauxetic effect can be described as the parameter β_1 , which was established by Brik *et al.*⁶³ And the value of β_1 can be calculated by the following expression:⁶⁸

$$\beta_1 = \sqrt{\left(\frac{B}{B_0}\right)^2 + \left(\frac{C}{C_0}\right)^2} \quad (8)$$

where $B_0 = 1160\text{ cm}^{-1}$ and $C_0 = 4303\text{ cm}^{-1}$, which was the Racah parameter of the free Mn^{4+} ions. Thus, the value of β_1 in the LaScO_3 host was about 0.924. Brik *et al.* also have presented the linear relationship [$E({}^2\text{E}_g) = -880.49 + 16\,261.92\beta_1 \pm \sigma$; $\sigma = 332\text{ cm}^{-1}$] between the ${}^2\text{E}_g$ energy level of Mn^{4+} ions in different hosts.⁶³ Fig. 4(a) depicts the relationship between the ${}^2\text{E}_g$ energy level of Mn^{4+} ions and β_1 in different hosts. All the points were located around the line $E({}^2\text{E}_g) = -880.49 + 16\,261.92\beta_1$, indicating the data were acceptable. The detailed data of these phosphors, which used in Fig. 4(a), were listed in Table 3. It can

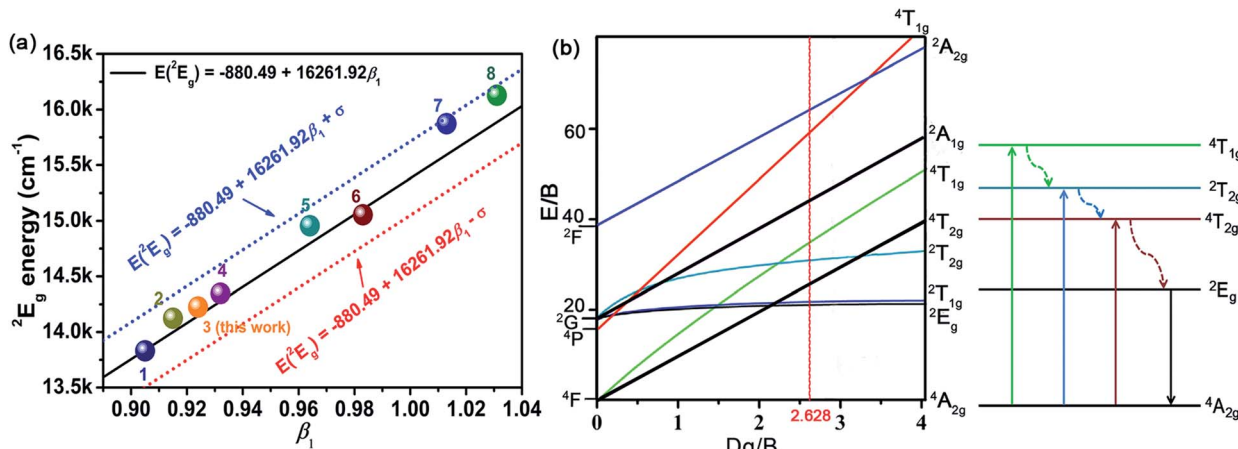


Fig. 4 (a) Dependence of the ${}^2\text{E}_g$ energy level of Mn^{4+} ions on the nephelauxetic ratio β_1 in different hosts including LaScO_3 [$E({}^2\text{E}_g) = -880.49 + 16\,261.92\beta_1 \pm \sigma$; $\sigma = 332\text{ cm}^{-1}$]. (b) (Left side) Tanabe–Sugano energy-level diagram of Mn^{4+} ions in the octahedral site of LaScO_3 host and (right side) the simple energy level diagram of Mn^{4+} ions.



Table 3 The spectroscopic parameters of Mn^{4+} ions in different host

No.	Hosts	Dq/cm^{-1}	$B\text{ cm}^{-1}$	C/cm^{-1}	Dq/B	β_1	$E(^2E_g)/cm^{-1}$	Ref.
1	$SiTiO_3$	1818	719	2839	2.529	0.905	13 831 (723 nm)	69
2	$La(MgTi)_{1/2}O_3$	2053	700	2959	2.933	0.915	14 124 (708 nm)	9
3	$LaScO_3$	1842	701	3006	2.628	0.924	14 225 (703 nm)	This work
4	$NaMgGdTeO_6$	2083	727	2971	2.865	0.932	14 347 (697 nm)	39
5	$Y_2Ti_2O_7$	2000	600	3500	3.333	0.964	14 956 (669 nm)	63 and 70
6	$CaZrO_3$	1850	754	3173	2.454	0.983	15 054 (664 nm)	67
7	K_2SiF_6	2197	599	3750	3.668	1.013	15 873 (630 nm)	63
8	$KTeF_5$	2267	567	3904	3.998	1.031	16 129 (620 nm)	71

be seen clearly from Table 3 and Fig. 4(a) that with the increasing of β_1 , the value of the energy level of 2E_g increased. And the value of the nephelauxetic effect in $LaScO_3:xMn^{4+}$ phosphors was close to the $La(MgTi)_{1/2}O_3:Mn^{4+}$, $NaMgGdTeO_6:Mn^{4+}$, and $SiTiO_3:Mn^{4+}$, indicating the similar coordination environments of Mn^{4+} ions in these phosphors. Based on the Tanabe–Sugano energy-level diagram in the left diagram of Fig. 4(b), the simple schematic diagram of the Mn^{4+} energy level transition in the $LaScO_3$ host was illustrated in the right diagram of Fig. 4(b). The electrons at the ground state $^4A_{2g}$ (from the 4F term) absorbed the energy of the excited light (398 nm or 549 nm) and then were pumped to the excited level $^4T_{1g}$ (from the 4F term), $^2T_{2g}$ (from the 2G term), and $^4T_{2g}$ (from the 4F term), after which the electrons could relax to the lowest excited state level 2E_g (from the 2G term) through non-radiative transitions process $^4T_{1g} \rightarrow ^2T_{2g} \rightarrow ^4T_{2g} \rightarrow ^2E_g$, and finally released the energy by radiation transitions process with a red light emission at 703 nm.⁶¹

Conclusions

In conclusion, $LaScO_3:xMn^{4+}$ ($x = 0.0005\text{--}0.009$) far-red emitting phosphors have been successfully synthesized via high-temperature solid-state reaction process. The crystal structure of the host and $LaScO_3:0.001Mn^{4+}$ phosphors had been discussed and the XRD patterns of the $LaScO_3:xMn^{4+}$ proved that they all were pure phase. Monitored at 703 nm, the obtained PLE spectrum of the $LaScO_3:0.001Mn^{4+}$ phosphors exhibited four Gaussian fitting peaks, centering at 346 nm ($28\ 902\text{ cm}^{-1}$; $Mn^{4+}\text{--}O^{2-}$ transition), 392 nm ($25\ 510\text{ cm}^{-1}$; $^4A_{2g} \rightarrow ^4T_{1g}$ dominant transition), 462 nm ($21\ 645\text{ cm}^{-1}$; $^4A_{2g} \rightarrow ^2T_{2g}$ transition), and 543 nm ($18\ 416\text{ cm}^{-1}$; $^4A_{2g} \rightarrow ^4T_{2g}$ transition). Upon 398 nm excitation, the PL spectrum of $LaScO_3:0.001Mn^{4+}$ phosphors showed a far-red emission peaking at 703 nm within the 650–800 nm range, which was very close to the central absorption wavelength of the P_{FR} at around 730 nm. The optimal doping concentration of Mn^{4+} ion was 0.001 in $LaScO_3$ host and the electric d-d interaction contributed to the concentration quenching mechanism. All the results indicated that the $LaScO_3:Mn^{4+}$ phosphors are promising far-red emitting materials for plant growth LEDs application.

Conflicts of interest

There are no conflicts to declare.

Acknowledgements

This work was supported by the National Natural Science Foundation of China (No. 51502190), the Program for the Outstanding Innovative Teams of Higher Learning Institutions of Shanxi, and the Open Fund of the State Key Laboratory of Luminescent Materials and Devices (South China University of Technology, No. 2017-skllmd-01).

Notes and references

- 1 R. J. Bula, R. C. Morrow, T. W. Tibbitts and D. J. Barta, *HortScience*, 1991, **26**, 203–205.
- 2 D. E. Macey and J. T. Arnott, *Can. J. For. Res.*, 1986, **16**, 949–954.
- 3 C. A. Jaleel, P. Manivannan, B. Sankar, A. Kishorekumar, R. Gopi, R. Somasundaram and R. Panneerselvam, *Colloids Surf., B*, 2007, **60**, 7–11.
- 4 C. Kami, S. Lorrain, P. Hornitschek and C. Fankhauser, *Curr. Top. Dev. Biol.*, 2010, **91**, 29–66.
- 5 L. Ma, D.-j. Wang, Z.-y. Mao, Q.-f. Lu and Z.-h. Yuan, *Appl. Phys. Lett.*, 2008, **93**, 144101.
- 6 J. Chen, N. Zhang, C. Guo, F. Pan, X. Zhou, H. Suo, X. Zhao and E. M. Goldys, *ACS Appl. Mater. Interfaces*, 2016, **8**, 20856–20864.
- 7 M. J. Kasperbauer, *Plant Physiol.*, 1987, **85**, 350–354.
- 8 P. F. Devlin, J. M. Christie and M. J. Terry, *J. Exp. Bot.*, 2007, **58**, 3071–3077.
- 9 Z. Zhou, J. Zheng, R. Shi, N. Zhang, J. Chen, R. Zhang, H. Suo, E. M. Goldys and C. Guo, *ACS Appl. Mater. Interfaces*, 2017, **9**, 6177–6185.
- 10 A. M. Srivastava, M. G. Brik, H. A. Comanzo, W. W. Beers, W. E. Cohen and T. Pocock, *ECS J. Solid State Sci. Technol.*, 2017, **7**, R3158–R3162.
- 11 T. Nakajima and T. Tsuchiya, *ACS Appl. Mater. Interfaces*, 2015, **7**, 21398–21407.
- 12 G. D. Massa, *HortScience*, 2008, **43**, 1951–1956.
- 13 H. Smith, *Nature*, 2000, **407**, 585–591.
- 14 X. Huang, *Nat. Photonics*, 2014, **8**, 748–749.
- 15 C. Yu, Z. Yang, J. Qiu, Z. Song and Z. Dacheng, *J. Am. Ceram. Soc.*, 2018, **101**, 612–623.
- 16 X. Wu, Y. Jiao, O. Hai, Q. Ren, F. Lin and H. Li, *J. Alloys Compd.*, 2018, **730**, 521–527.

17 J. Han, L. Li, M. Peng, B. Huang, F. Pan, F. Kang, L. Li, J. Wang and B. Lei, *Chem. Mater.*, 2017, **29**, 8412–8424.

18 D. Wen, H. Kato, M. Kobayashi, S. Yamamoto, M. Mitsuishi and M. Kakihana, *J. Mater. Chem. C*, 2017, **5**, 4578–4583.

19 P. Du, L. Luo, X. Huang and J. S. Yu, *J. Colloid Interface Sci.*, 2018, **514**, 172–181.

20 P. Du, X. Huang and J. S. Yu, *Inorg. Chem. Front.*, 2017, **4**, 1987–1995.

21 X. Huang, *J. Alloys Compd.*, 2017, **690**, 356–359.

22 H. Guo, X. Huang and Y. Zeng, *J. Alloys Compd.*, 2018, **741**, 300–306.

23 P. Du, X. Huang and J. S. Yu, *Chem. Eng. J.*, 2018, **337**, 91–100.

24 X. Huang and H. Guo, *Dyes Pigm.*, 2018, **154**, 82–86.

25 S. G. Prasanna Kumar, R. Hari Krishna, N. Kottam, P. Krishna Murthy, C. Manjunatha, R. Preetham, C. Shivakumara and T. Thomas, *Dyes Pigm.*, 2018, **150**, 306–314.

26 J. Zhong, S. Zhou, D. Chen, J. Li, Y. Zhu, X. Li, L. Chen and Z. Ji, *Dalton Trans.*, 2018, **47**, 8248.

27 X. Huang, H. Guo and B. Li, *J. Alloys Compd.*, 2017, **720**, 29–38.

28 X. Huang, B. Li, H. Guo and D. Chen, *Dyes Pigm.*, 2017, **143**, 86–94.

29 H. Guo, B. Devakumar, B. Li and X. Huang, *Dyes Pigm.*, 2018, **151**, 81–88.

30 X. Huang, S. Wang, B. Li, Q. Sun and H. Guo, *Opt. Lett.*, 2018, **43**, 1307–1310.

31 L. Y. Wang, E. H. Song, T. T. Deng, Y. Y. Zhou, Z. F. Liao, W. R. Zhao, B. Zhou and Q. Y. Zhang, *Dalton Trans.*, 2017, **46**, 9925–9933.

32 G. Zhu, Z. Li, C. Wang, F. Zhou, Y. Shi, Y. Wen and S. Xin, *J. Mater. Sci.: Mater. Electron.*, 2017, **29**, 2216–2221.

33 R. Cao, M. Peng, E. Song and J. Qiu, *ECS J. Solid State Sci. Technol.*, 2012, **1**, R123–R126.

34 Q. Sun, S. Wang, B. Li, H. Guo and X. Huang, *J. Lumin.*, 2018, **203**, 371–375.

35 J. Liang, P. Du, H. Guo, L. Sun, B. Li and X. Huang, *Dyes Pigm.*, 2018, **157**, 40–46.

36 K. Sankarasubramanian, B. Devakumar, G. Annadurai, L. Sun, Y.-J. Zeng and X. Huang, *RSC Adv.*, 2018, **8**, 30223–30229.

37 X. Huang, J. Liang, B. Li, L. Sun and J. Lin, *Opt. Lett.*, 2018, **43**, 3305–3308.

38 M. Peng, X. Yin, P. A. Tanner, M. G. Brik and P. Li, *Chem. Mater.*, 2015, **27**, 2938–2945.

39 K. Li, H. Lian and R. V. Deun, *J. Lumin.*, 2018, **198**, 155–162.

40 X. Huang and H. Guo, *Dyes Pigm.*, 2018, **152**, 36–42.

41 Y. Takeda, H. Kato, M. Kobayashi, H. Kobayashi and M. Kakihana, *Chem. Lett.*, 2015, **44**, 1541–1543.

42 R. Cao, W. Luo, Q. Xiong, S. Jiang, Z. Luo and J. Fu, *Chem. Lett.*, 2015, **44**, 1422–1424.

43 D. Lybye, P. Finn Willy and M. Mogens, *Solid State Ionics*, 2000, **128**, 91–103.

44 J. Du, O. Q. De Clercq, K. Korthout and D. Poelman, *Materials*, 2017, **10**, 1422.

45 C. Wu, J. Li, H. Xu, J. Wu, J. Zhang, Z. Ci, L. Feng, C. Cao, Z. Zhang and Y. Wang, *J. Alloys Compd.*, 2015, **646**, 734–740.

46 M. H. Du, *J. Mater. Chem. C*, 2014, **2**, 2475–2481.

47 L. Qin, S. Bi, P. Cai, C. Chen, J. Wang, S. I. Kim, Y. Huang and H. J. Seo, *J. Alloys Compd.*, 2018, **755**, 61–66.

48 R. Cao, Z. Shi, G. Quan, T. Chen, S. Guo, Z. Hu and P. Liu, *J. Lumin.*, 2017, **188**, 577–581.

49 R. Cao, Y. Ye, Q. Peng, G. Zheng, H. Ao, J. Fu, Y. Guo and B. Guo, *Dyes Pigm.*, 2017, **146**, 14–19.

50 B. Wang, H. Lin, F. Huang, J. Xu, H. Chen, Z. Lin and Y. Wang, *Chem. Mater.*, 2016, **28**, 3515–3524.

51 B. Wang, H. Lin, J. Xu, H. Chen and Y. Wang, *ACS Appl. Mater. Interfaces*, 2014, **6**, 22905–22913.

52 U. B. Humayoun, S. N. Tiruneh and D.-H. Yoon, *Dyes Pigm.*, 2018, **152**, 127–130.

53 M. Inokuti and F. Hirayama, *J. Chem. Phys.*, 1965, **43**, 1978–1989.

54 S. Zhang, Y. Hu, H. Duan, Y. Fu and M. He, *J. Alloys Compd.*, 2017, **693**, 315–325.

55 B. Li, X. Huang, H. Guo and Y. Zeng, *Dyes Pigm.*, 2018, **150**, 67–72.

56 X. Huang, B. Li and H. Guo, *J. Alloys Compd.*, 2017, **695**, 2773–2780.

57 K. Li, H. Lian and R. Van Deun, *Dalton Trans.*, 2018, **47**, 2501–2505.

58 C. Wang, Y. Jin, Y. Lv, G. Ju, L. Chen, Z. Li and Y. Hu, *J. Lumin.*, 2017, **192**, 337–342.

59 S. K. Hussain, T. T. H. Giang and J. S. Yu, *J. Alloys Compd.*, 2018, **739**, 218–226.

60 S. Liang, M. Shang, H. Lian, K. Li, Y. Zhang and J. Lin, *J. Mater. Chem. C*, 2016, **4**, 6409–6416.

61 X. Zhang, J. Nie, S. Liu, Y. Li and J. Qiu, *J. Am. Ceram. Soc.*, 2017, 1–9.

62 C. Yang, Z. Zhang, G. Hu, R. Cao, X. Liang and W. Xiang, *J. Alloys Compd.*, 2017, **694**, 1201–1208.

63 M. G. Brik, S. J. Camardello and A. M. Srivastava, *ECS J. Solid State Sci. Technol.*, 2014, **4**, R39–R43.

64 L. Zhou, C. Shen, L. Shen, S. Liu, J. Liu, L. Ding, J. Du, W. Xiang and X. Liang, *J. Alloys Compd.*, 2018, **769**, 686–693.

65 J. Zhong, D. Chen, S. Yuan, M. Liu, Y. Yuan, Y. Zhu, X. Li and Z. Ji, *Inorg. Chem.*, 2018, **57**, 8978–8987.

66 Z. Lu, H. Wang, D. Yu, T. Huang, L. Wen, M. Huang, L. Zhou and Q. Wang, *Opt. Laser Technol.*, 2018, **108**, 116–123.

67 M. G. Brik and A. M. Srivastava, *ECS J. Solid State Sci. Technol.*, 2013, **2**, R148–R152.

68 M. G. Brik, S. J. Camardello, A. M. Srivastava, N. M. Avram and A. Suchocki, *ECS J. Solid State Sci. Technol.*, 2015, **5**, R3067–R3077.

69 Z. Bryknar, V. Trepakov, Z. Potůček and L. Jastrabík, *J. Lumin.*, 2000, **87–89**, 605–607.

70 M. G. Brik, A. M. Srivastava and N. M. Avram, *Opt. Mater.*, 2011, **33**, 1671–1676.

71 T. T. Deng, E. H. Song, J. Su, Y. Y. Zhou, L. Y. Wang, S. Ye and Q. Y. Zhang, *J. Mater. Chem. C*, 2018, **6**, 4418–4426.

